electronic reprint

Journal of
Applied Crystallography
ISSN 0021-8898
Editor: **Gernot Kostorz**

A direct method for the determination of the mean orientation-dependent elastic strains and stresses in polycrystalline materials from strain pole figures

Joel V. Bernier and Matthew P. Miller

Journal of
Applied Crystallography
ISSN 0021-8898

Received 19 July 2005
Accepted 16 March 2006

A direct method for the determination of the mean orientation-dependent elastic strains and stresses in polycrystalline materials from strain pole figures

Joel V. Bernier[a]* and Matthew P. Miller[b]

[a]The Advanced Photon Source, Argonne National Laboratory, Argonne, IL 60439, USA, and [b]Sibley School of Mechanical and Aerospace Engineering, Cornell University, Ithaca, NY 14853, USA. Correspondence e-mail: jvb7@cornell.edu

A salient manifestation of anisotropy in the mechanical response of polycrystalline materials is the inhomogeneous partitioning of elastic strains over the aggregate. For bulk samples, the distributions of these intergranular strains are expected to have a strong functional dependence on grain orientations. It is then useful to formulate a mean lattice strain distribution function (LSDF) over the orientation space, which serves to characterize the micromechanical state of the aggregate. Orientation-dependent intergranular stresses may be recovered from the LSDF *via* a constitutive assumption, such as anisotropic linear elasticity. While the LSDF may be determined directly from simulation data, its experimental determination relies on solving an inverse problem that is similar in character to the fundamental problem of texture analysis. In this paper, a versatile and robust direct method for determining an LSDF from strain pole figures is presented. The effectiveness of this method is demonstrated using synthetic strain pole figures from a model LSDF obtained from the simulated uniaxial deformation of a 1000-crystal aggregate.

1. Introduction

In polycrystalline materials, such as structural alloys, macroscopically imposed strain and stress are partitioned among the constituent grains in a complex inhomogeneous manner. This phenomenon may be attributed to both the anisotropy of the individual grains and the complex mechanical state imposed by interactions with neighboring grains. The ability to quantify experimentally the inhomogeneity of strain/stress partitioning and correlate it with structure-based modeling results is critical to the understanding of various deformation processes in polycrystalline materials. For instance, highly stressed crystals (with respect to some mean) may act as nucleation sites for many performance-limiting processes such as fatigue. Other phenomena important to materials processing, such as recrystallization and phase transformation, are also highly sensitive to the local state of stress.

Diffraction methods can provide grain-scale measurements of normal strains for samples that have been thermomechanically processed *ex situ* (residual strain) as well as *in situ*. Stresses may be correlated with these strains *via* constitutive assumptions, such as (anisotropic) linear elasticity. Experimental measurements of aggregate-averaged lattice strains *via* established diffraction-based residual stress techniques are quite valuable for understanding variations in mechanical state from one continuum point (aggregate of grain) to the next (Lu, 1996; Hauk, 1997). Data from *in situ* experiments, however, provide information on the evolution of micromechanical state during thermomechanical processing, which may in turn be compared directly with simulation results as in the work of Dawson *et al.* (2001) and Han & Dawson (2005). While aggregate sizes were traditionally limited to the continuum level, the recent availability of high-energy high-brilliance synchrotron X-rays has allowed for the development of point-wise measurements of orientation and strain within single embedded grains (Poulsen *et al.*, 2001; Margulies *et al.*, 2002).

The latter techniques have great promise for understanding intragranular deformation phenomena and local inhomogeneity of strain/stress; however, they are not suitable for surveying grain populations large enough to assess intergranular inhomogeneities over statistically representative volumes. The ability to predict reliably statistical distributions of intergranular inhomogeneity is of primary importance to the modeling of anisotropy in fundamental mechanical properties, such as macroscopic strength and stiffness (Dawson *et al.*, 2005; Han & Dawson, 2005). As such, the focus of the present work is the interpretation of intergranular strain/stress from powder diffraction experiments such as described by Carter & Bourke (2000), Wanner & Dunand (2000) and Miller *et al.* (2005).

At the scale of statistically representative grain populations (*i.e.* well approximated by a continuum), the crystal strains are expected to be a strong, though non-unique, function of orientation. Variations in the micromechanical states among grains having crystallographically equivalent orientations

arise from spatial variations in attributes such as their morphologies, as well as the number, orientations, morphologies and compositions of neighboring grains.

Recently the concept of an orientation-dependent crystal strain/stress tensor field, *i.e.* a strain/stress orientation distribution function (SODF), has been proposed in order to quantify the micromechanical state of polycrystalline materials at the intergranular level (Behnken, 2000; Wang *et al.*, 2001; Popa & Balzar, 2001). By construction, the SODF is defined over the fundamental region of orientation space associated with the symmetries of the crystal and sample reference frames. This intrinsic symmetry suggests the interpretation of the SODF as a mean strain/stress field as a function of grain orientation. As a result, information regarding the variance in micromechanical state among grains having symmetrically equivalent orientations is omitted.

For clarity, the authors have chosen to adopt the terms lattice strain distribution function (LSDF) for the elastic strain field and SODF for the corresponding stress field. The SODF may be determined from the LSDF *via* anisotropic linear elasticity. The benefits of LSDF analysis go beyond explaining diffraction line shifts for strained specimens; the method provides a compact description of the orientation-dependent micromechanical state in bulk samples. When coupled with experiments in which samples are deformed *in situ*, the LSDF may prove invaluable for both the validation and the development of structure-based material models.

The construction of an LSDF from experimentally measured lattice strain data is an inherently indeterminate problem (see §4). Because of this fundamental difficulty, it is insufficient simply to find an LSDF that represents the 'best fit' of the measured data for quantitative analysis. Additional conditions and/or constraints must be imposed in solving the problem to ensure a feasible and unique solution. Furthermore, it is desirable that these mathematical modeling assumptions be formulated independently of any kinematic modeling assumptions (such as Voight, Reuss or self-consistent) to minimize solution bias. Any viable method must also be robust in the presence of experimental noise in the measured data.

We propose obtaining an LSDF as the solution to a well posed auxiliary problem of unconstrained optimization. This work provides several novel contributions to the area:

(i) an objective function that provides a robust solution method based on single-crystal constitutive behavior,

(ii) a direct discretization scheme as an alternative to the spherical harmonics approaches introduced by Wang *et al.* (2001), Behnken (2000) and Popa & Balzar (2001), and

(iii) an evaluation of performance using a simulated LSDF from an elasto-viscoplastic polycrystal model.

2. Measurement of lattice strains

Normal lattice strains are measured *via* diffraction techniques, and their relationship to the LSDF is presented in this context. Mean strains over the diffraction volume are manifested as line shifts, while the variation about the mean may be correlated with line broadening (Young, 1995; Cullity, 1978). The present paper presents a method for interpreting the former quantity.

Bragg's law relates the average spacing, $\bar{d}_{\mathbf{c}}$, of lattice planes having normal $\mathbf{c}$ to the scattering angle, θ, and wavelength, λ, of the probing radiation:

$$n\lambda = 2\bar{d}_{\mathbf{c}} \sin\theta \quad \text{for} \quad n = 1, 2, 3, \ldots \tag{1}$$

For measurements associated with the sample-relative direction, $\mathbf{s}$, the average in equation (1) refers to the subset of grains in the diffraction volume having orientations, R', that satisfy

$$\mathsf{R}'\mathbf{c} = \pm\mathbf{s}. \tag{2}$$

The collection of all scattering vectors, $\mathbf{s}$, defines the pole figure. The antipodal symmetry of the pole figure implied by equation (2) is a consequence of Friedel's law.

If a reference plane spacing, $d^0_{\mathbf{c}}$, is available (*e.g.* from a measurement of the unstrained lattice parameters), the lattice strain may be defined as

$$\tilde{\epsilon}_{\mathbf{c}}(\mathbf{s}) \equiv (\bar{d}_{\mathbf{c}} - d^0_{\mathbf{c}})/d^0_{\mathbf{c}}, \tag{3}$$

where $\mathbf{c}$ and $\mathbf{s}$ are related by equation (2). If lattice strains associated with the crystallographic direction $\mathbf{c}$ are measured for a sufficiently large number of distinct $\mathbf{s}$, then $\tilde{\epsilon}_{\mathbf{c}}(\mathbf{s})$ may be represented as a generalized pole figure. The resulting scalar field is referred to as a strain pole figure (SPF).

Since the partitioning of macroscopic strains (including residual strains) is generally three-dimensional, it is the goal of experimental methods to maximize both the number and the $\mathbf{s}$ coverage of SPFs (Miller *et al.*, 2005). The reciprocal-space coverage and fidelity of SPF data has a major effect on the ability to correlate the measurements to an LSDF.

3. The lattice strain distribution function (LSDF)

The LSDF, $\boldsymbol{\epsilon}(\mathsf{R})$, is a symmetric second-rank tensor field on the orientation space that represents the average strain tensor for the volume fraction of the polycrystal having orientation R. It is intimately related to the orientation distribution function (ODF[1]):

$$\mathrm{d}V_{\mathcal{B}}/V_{\mathcal{B}} \equiv V_{\Omega}^{-1} f(\mathsf{R})\,\mathrm{d}\mathsf{R}, \tag{4}$$

with

$$V_{\Omega}^{-1} \int_{\Omega} f(\mathsf{R})\,\mathrm{d}\mathsf{R} = 1 \quad \text{and} \quad f \geq 0, \tag{5}$$

where $V_{\mathcal{B}}$ and V_{Ω} represent the volumes of the polycrystal (more specifically, the diffraction volume) and orientation space, respectively (Bunge, 1982). The average macroscopic elastic strain tensor over $V_{\mathcal{B}}$, $\bar{\boldsymbol{\epsilon}}$, is then obtained as

$$\bar{\boldsymbol{\epsilon}} = V_{\Omega}^{-1} \int_{V_{\Omega}} \boldsymbol{\epsilon}(\mathsf{R}) f(\mathsf{R})\ \mathrm{d}\mathsf{R}. \tag{6}$$

Note that the LSDF is not a probability density function like the ODF, but is a non-spatial orientation-dependent mean

[1] Also referred to as the CODF by Behnken (2000), Wang *et al.* (2001) and Popa & Balzar (2001).

strain field. As a result, the LSDF need not represent a compatible deformation. There are also no explicit mathematical constraints in the form of equation (5) on the LSDF.

LSDF analysis provides a strictly statistical description of the micromechanical state in a polycrystalline material. As such, it may only be defined for statistically representative volumes within the sample. The authors propose the use of the ODF to determine the feasibility of applying an LSDF; samples that may be well characterized by an ODF (*i.e.* relative pole-figure errors below ∼10%) should contain a statistically relevant number of grains for LSDF analysis. In general, there will be an ODF and an LSDF associated with each phase[2] present in the polycrystal.

The SODF as defined by Behnken (2000) and Wang *et al.* (2001) is related to the LSDF by a constitutive relation. If observed line shift is assumed to be purely elastic, then anisotropic linear elasticity may be applied:

$$\boldsymbol{\sigma}_i(\mathsf{R}) = \mathbb{C}_{ij}(\mathsf{R})\,\boldsymbol{\epsilon}_j(\mathsf{R}), \tag{7}$$

where $\mathbb{C}$ is the crystal elastic stiffness tensor. Just as the LSDF need not satisfy compatibility, an SODF derived from a particular LSDF *via* equation (7) need not satisfy equilibrium owing to the lack of any spatial correlation of the SODF with the diffraction volume.

3.1. Symmetry

Both the LSDF and the SODF are defined over the orientation space and inherit its symmetries by construction. As a result, they may be completely described over the fundamental region, $\Omega_{\rm fr}$, associated with the crystal and sample symmetries. Popa & Balzar (2001) have proposed an alternative invariance condition, where only the experimentally observed scalar quantity, $\bar{d}_{\mathbf{c}}$, is invariant. The treatment proposed herein is functionally equivalent as the symmetric invariance of $\bar{d}_{\mathbf{c}}$ is ensured by the invariance of the underlying LSDF. This invariance follows from the fact that $\bar{d}_{\mathbf{c}}$ represents an averaged set of normal projections of the LSDF, an operation that preserves symmetry (see §3.2).

As tensor fields, the components of the LSDF must be written relative to a particular choice of basis. The sample-relative frame is chosen to write all tensor components herein. By this convention, the tensor components of the LSDF are identical at symmetrically equivalent orientations under the crystal symmetry. The effect of statistical symmetries in the sample frame, however, is slightly more complicated; the relationships between tensor components at orientations equivalent under combined crystal and sample symmetries has been described for several specific cases by Wang (2000). For a particular sample symmetry, denoted by the rotation H, under the chosen convention for writing tensor components we obtain

$$\boldsymbol{\epsilon}_{ij}(\mathsf{R}^*) = \mathsf{H}_{ik}\,\boldsymbol{\epsilon}_{kl}(\mathsf{R})\,\mathsf{H}_{jl}, \tag{8}$$

where $\mathsf{R}^* = \mathsf{HR}$. Therefore, the action of the sample symmetries on the components of the LSDF is analogous to a change of basis.

3.2. Relationship to the SPF

The relationship between the LSDF and SPFs is directly analogous to the fundamental relationship of quantitative texture analysis (QTA). For reference, the pole density function, $\tilde{P}_{\mathbf{c}}(\mathbf{s})$, indicates the volume fraction of the polycrystal that satisfies each a particular Bragg condition [equation (2)]:

$$\mathrm{d}V_{\mathcal{B}}/V_{\mathcal{B}} \equiv (4\pi)^{-1}\tilde{P}_{\mathbf{c}}(\mathbf{s})\,\mathrm{d}\mathbf{s}, \tag{9}$$

with

$$(4\pi)^{-1}\int_{\mathcal{S}^2}\tilde{P}_{\mathbf{c}}(\mathbf{s})\,\mathrm{d}\mathbf{s} = 1 \quad \text{and} \quad \tilde{P} \geq 0. \tag{10}$$

The ODF is related to the pole density function (PDF) by the integral projection (Bunge, 1982)

$$\tilde{P}_{\mathbf{c}}(\mathbf{s}) = \frac{1}{2\pi}\left\langle \oint_{\mathsf{R}(\theta)\mathbf{c}=\pm\mathbf{s}} f\,\left|\mathrm{d}\mathsf{R}/\mathrm{d}\theta\right|\mathrm{d}\theta \right\rangle, \tag{11}$$

where $\langle\cdots\rangle$ implies the mean of the integrals over each orientation fiber, $\mathsf{R}(\theta)\mathbf{c} = \pm\mathbf{s}$, and θ parameterizes the arc length. The SPF is similarly related to the LSDF as

$$\tilde{\epsilon}_{\mathbf{c}}(\mathbf{s}) = \frac{\left\langle \oint_{\mathsf{R}(\theta)\mathbf{c}=\pm\mathbf{s}} \mathbf{s}\cdot\boldsymbol{\epsilon}\cdot\mathbf{s}\, f\,\left|\mathrm{d}\mathsf{R}/\mathrm{d}\theta\right|\mathrm{d}\theta \right\rangle}{\left\langle \oint_{\mathsf{R}(\theta)\mathbf{c}=\pm\mathbf{s}} f\,\left|\mathrm{d}\mathsf{R}/\mathrm{d}\theta\right|\mathrm{d}\theta \right\rangle} \tag{12}$$

$$\equiv \left[\tilde{N}_{\mathbf{c}}\boldsymbol{\epsilon}\right](\mathbf{s}), \tag{13}$$

where the ODF is used as a weighting function and the denominator is the associated PDF value [equation (11)]. While equation (12) is linear in $\boldsymbol{\epsilon}$, its solution is indeterminate. A procedure for solving equation (12) for the LSDF, referred to as strain pole-figure inversion, is the main focus of this paper.

4. SPF inversion methods

The fundamental function of any SPF inversion method is to find an LSDF that describes the SPF data in an optimal sense. For quantitative strain analysis, however, this condition alone is insufficient. A viable SPF inversion method must also be robust, particularly in the presence of experimental errors. To date, a direct assessment of the robustness of the various SPF inversion methods has not been reported. This issue has received much attention in QTA, particularly following the discovery of 'ghost' phenomena in the original Fourier approaches (Matthies & Vinel, 1982). The reader is referred to Kallend (2000) for a comprehensive overview of the PDF inversion problem, which shares many similarities with SPF inversion. Bernier *et al.* (2006) have recently proposed a novel PDF inversion method designed to address a lack of robust-

[2] 'Phase' in this context is meant to imply a crystal structure that is distinguishable by diffraction methods.

ness observed in several commonly implemented methods. A similar approach, based on those results, is presented here for the task of SPF inversion.

The indeterminacy of equation (12) must be handled by defining a well posed auxiliary problem, where additional conditions and/or constraints are enforced on the solution. As there are no model-independent constraints on the LSDF, any mathematical modeling assumptions are purely heuristic. A natural choice for the auxiliary problem is one of optimization. Wang *et al.* (2001) and Behnken (2000) have pursued this approach, proposing objective functions that combine residuals on the N measured ($\tilde{\epsilon}^{\rm M}_{\mathbf{c}}$) and reconstructed SPFs [equation (13)],

$$r_{\tilde{\epsilon}} \equiv \sum_{i=1}^{N} \parallel \tilde{\epsilon}^{\rm M}_{\mathbf{c}_i} - \tilde{N}_{\mathbf{c}_i}\boldsymbol{\epsilon} \parallel^2, \tag{14}$$

with additional terms designed to enforce certain conditions on the trial solution. Typically these terms are weighted by non-negative coupling parameters. The authors note that the choice of additional conditions is non-trivial, as they are bound to have a profound influence on the character of the 'optimal' solution. Ideally, additional conditions on the LSDF should be based on physical behavior independent of kinematic modeling assumptions, such as Voight, Reuss or self-consistent. These conditions must also provide robustness, in terms of both noise filtering and the consistency of solutions with refinement of the discretization. Note that, because the LSDF has no direct spatial correlation, compatibility cannot be enforced as a constraint in the traditional sense.

Behnken (2000) has proposed a host of additional terms, including the strain variance,

$$\int_{V_\Omega} (\boldsymbol{\epsilon} - \bar{\boldsymbol{\epsilon}})^2 \, \mathrm{dR}, \tag{15}$$

the stress variance and the variance in orientation-dependent strain energy,

$$\int_{V_\Omega} (\boldsymbol{\sigma} : \boldsymbol{\epsilon} - \bar{\boldsymbol{\sigma}} : \bar{\boldsymbol{\epsilon}})^2 \, \mathrm{dR}. \tag{16}$$

Wang *et al.* (2001) have proposed a term based on the deviation of the SODF from the self-consistent stress state as determined from the ODF. Results from the application of these methods to measured data are given by Behnken (2000) and Wang *et al.* (2001, 2002, 2003).

4.1. New method

In the proposed method, the inversion problem for N SPFs is cast as an unconstrained optimization problem with the following objective:

$$\min_{\boldsymbol{\epsilon}} \left(r^{\rm w}_{\tilde{\epsilon}} + \alpha \parallel \nabla\boldsymbol{\epsilon} \parallel^2_{\Omega_{\rm fr}} + \beta \parallel \nabla \mathrm{Tr}\,\boldsymbol{\epsilon} \parallel^2_{\Omega_{\rm fr}} \right) \quad \text{for } \alpha, \beta \geq 0, \tag{17}$$

where $\parallel \cdots \parallel^2_{\Omega_{\rm fr}}$ represents the standard squared-integral norm over the fundamental region of the orientation space, $\Omega_{\rm fr}$, and $r^{\rm w}_{\tilde{\epsilon}}$ is the weighted SPF residual:

$$r^{\rm w}_{\tilde{\epsilon}} \equiv \sum_{i=1}^{N} \parallel \tilde{P}_{\mathbf{c}_i} \tilde{\epsilon}^{\rm M}_{\mathbf{c}_i} - \tilde{N}^{\rm w}_{\mathbf{c}_i}\boldsymbol{\epsilon} \parallel^2, \tag{18}$$

with

$$\tilde{N}^{\rm w}_{\mathbf{c}} \equiv \tilde{P}_{\mathbf{c}} \cdot \tilde{N}_{\mathbf{c}}. \tag{19}$$

The use of a weighted SPF residual reflects the inherently statistical nature of $\boldsymbol{\epsilon}$; *i.e.* for textured polycrystals, the most relevant strains, in terms of both the fidelity of the measurements and their relative impact on the macrostress/strain, are those measured for orientations that represent the largest volume fractions of the aggregate. Popa & Balzar (2001) have also implicitly suggested the use of a weighted SPF residual in their approach.

Note that the case where $\alpha, \beta = 0$ in equation (17) would yield a solution that optimally describes the input SPFs, although in the absence of direct conditional control on the LSDF. Equation (17) is independent of any particular choice of parameterization and representation of the orientation space, and may be written as a quadratic form in $\boldsymbol{\epsilon}$.

The use of gradient-based diffusive terms for solution stability is well established in numeric methods for the solution of hyperbolic PDEs (Johnson, 1992). The α term is included for this purpose, recognizing that random noise is unavoidable in the measured SPFs, $\tilde{\epsilon}^{\rm M}_{\mathbf{c}_i}$; sources of experimental errors include statistical fluctuations in the sample and resolution limits for determining diffraction line positions (Withers *et al.*, 2001). Bernier *et al.* (2006) have recently proposed a similar term in a dual objective for PDF inversion, which has produced favorable results.

The β term penalizes large gradients in the volumetric component (*i.e.* the dilatation) of $\boldsymbol{\epsilon}$. As a tensor invariant, $\mathrm{Tr}\,\boldsymbol{\epsilon}$ also appears in the α term; the β term, however, provides an independent means of control. This condition effectively favors trial solutions with uniform dilatations. Although this may lead to an artificial homogenization of the solution, penalizing the gradient-norm of the dilatation is empirically shown to improve global accuracy in $\boldsymbol{\epsilon}$ (see §5). The trial solution is also expected to capture accurately the volume-averaged dilatation.

In addition, the largest arena for LSDF/SODF analysis is presumably structural materials, the vast majority of which display decoupling between their volumetric and deviatoric elastic responses at the single-crystal level. This includes all cubic (O_h) and many hexagonal close packing (h.c.p.) (D_{6h}) alloys. As the dilatation alone is an inherently isotropic response, its variation over the polycrystal should be relatively small compared with the deviatoric response and dominated by spatial variations in grain neighborhood rather than grain orientation. By penalizing the gradient norm of the dilatation, solutions having small variance in that component are biased. This condition is purely mathematical and is intended to avoid biasing the solution with respect to any kinematic modeling assumptions, such as minimizing the deviation from a self-consistent stress state (Wang *et al.*, 2001).

The fact that the form of both conditional terms in equation (17) allows the problem to be written as a quadratic form in $\boldsymbol{\epsilon}$

significantly improves computational efficiency. The authors note that an *a priori* selection criteria for the free parameters α and β is desirable but quite difficult to formulate for the general case. Wang *et al.* (2001) have made a similar observation, proposing that the coupling parameter in their dual objective be chosen such that the relative error between the input and reconstructed SPFs is approximately 10% larger than if the coupling term were 0. A similar approach is suggested here in §8, on the basis of the results of a parameter study with a model LSDF (see §5).

4.2. Parameterization and representation

The approaches of Behnken (2000), Wang *et al.* (2001) and Popa & Balzar (2001) rely on Euler angle parameterizations of the orientation space and generalized spherical harmonics for representation of the LSDF and SPFs. This choice of parametrization and representation is pervasive in QTA as well.

The choice of parametrization should provide a straightforward geometric representation of $\Omega_{\rm fr}$ to exploit symmetries fully. Benefits of interpolation functions with global support, such as spherical harmonics, include the ability to represent symmetries exactly at every point in the domain, while locally defined interpolation functions such as FE (finite elements) allow for local control of resolution.

In this paper, the SPF inversion method is implemented using Rodrigues parameters for the orientation space and finite elements for the representation of functions. The use of Rodrigues and other angle–axis parameterizations has been proposed in the context of QTA (Frank, 1988; Heinz & Neumann, 1991; Morawiec & Field, 1996; Kumar & Dawson, 1998; Barton *et al.*, 2002; Bernier *et al.*, 2006). In the Rodrigues parameterization, an orientation is represented by the vector

$$\mathbf{r} = \mathbf{n} \tan \varphi/2, \tag{20}$$

where $\boldsymbol{n}$ and φ are the axial vector and angle of the associated rotation matrix, respectively. Many operations are simplified in angle–axis parameterizations, including the calculation of the integration paths in equations (11) and (12). In addition, the $\Omega_{\rm fr}$ associated with common crystal and/or sample symmetries are convex polyhedra in Rodrigues space, which are readily discretized. The metric is also non-singular in the $\Omega_{\rm fr}$ for most[3] Laue groups, including those most common to engineering materials. The same properties are not necessarily true for the Euler spaces.

Finite elements have also been proposed for representation of functions in QTA (Schaeben, 1991; Kumar & Dawson, 1998; Barton *et al.*, 2002; Bernier *et al.*, 2006). The use of FE has many benefits, including continuous representation of functions, sparse matrix representations of integral operators such as $\tilde{\mathbf{M}}$ and high-accuracy numerical integration. One distinct advantage over other direct discretization schemes, such as cells, is the ability to calculate gradients with high accuracy. When coupled with the use of Rodrigues parameterization, as done by Kumar & Dawson (1998), Barton *et al.* (2002) and Bernier *et al.* (2006), these features provide an efficient framework for LSDF/SODF analysis. Symmetries are readily handled *via* nodal point equivalences, as described by Kumar & Dawson (1998), Barton *et al.* (2002) and Bernier *et al.* (2006). Linear tetrahedral elements are utilized exclusively in the present work, largely because of the simplicity of constructing meshes *via* Delaunay triangulation and their ease of implementation. In these elements, the interpolation function values at an interior point of an element are identical to the barycentric coordinates of the point in the element.

4.3. The discrete spherical harmonics

Two of the most attractive features of spherical harmonics (*i.e.* a discretization scheme with global support) for representing functions are computational economy and noise filtering. The representation of symmetries and the numerical evaluation of integrals, however, is often more straightforward in direct discretization schemes with local support (*e.g.* cells, FE). Direct discretization schemes of sufficient resolution, however, are typically more susceptible to high-frequency noise.

The authors have recently presented a methodology for performing a mapping between the two discretization schemes using the FE/Rodrigues framework in order to exploit fully the benefits of each scheme (Bernier *et al.*, 2006). The generalized eigenfunctions of the FE gradient inner product operator provide nodal point approximations to the real, symmetrized spherical harmonics on the mesh over $\Omega_{\rm fr}$. These discrete eigenfunctions may be used as *global* interpolation functions on the mesh, with the local FE degrees of freedom (DOF) being mapped 1:1 to a discrete set of harmonic coefficients. Because the discrete harmonic modes are defined at every nodal point, functions may be represented on the mesh using only a fraction of the total FE DOF. Observe that for the L lowest-order modes (sorted by their associated eigenvalues), V_i, the nodal point values of a function on the mesh, $\{x\}_{\rm NP}$, are recovered from the coefficients, c_i as a matrix–vector multiplication:

$$\{x\}_{\rm NP} = \left[\{V_1\}_{\rm NP}\, \{V_2\}_{\rm NP}\, \ldots\, \{V_L\}_{\rm NP}\right] \begin{Bmatrix} c_1 \\ c_2 \\ \vdots \\ c_L \end{Bmatrix}. \tag{21}$$

In addition to economy of representation, the attractive low-pass noise filtering traits and economy associated with low-order harmonic expansions may be effectively included in the FE/Rodrigues representation. Symmetries are enforced *via* the nodal point equivalences on the underlying mesh. The discrete harmonics may be calculated for functions with multiple DOF per nodal point, such as the LSDF.

5. Example: simulated SPF data

A simulated SPF inversion problem is presented to demonstrate the effectiveness of equation (17) in recovering an

[3] Exceptions include $\bar{1}$, $2/m$, $4/m$, $\bar{3}$ and $6/m$. For these groups, the unit quaternion parameterization may be used in lieu of Rodrigues'.

LSDF that is known *a priori*. As point-wise measurements of lattice strain for large populations of embedded grains are not yet available, simulated distributions provide the only 'direct' means of validation for SPF inversion methods. Similar approaches have been employed to validate PDF-to-ODF inversion methods (Van Houtte, 1984; Matthies *et al.*, 1988; Caleyo *et al.*, 2001; Bernier *et al.*, 2006). The authors note that some care must be taken in pursuing such a comparison to avoid biasing the results to suit the inversion method. For example, a model LSDF obtained *via* an elasto-viscoplastic Taylor calculation provides an ideal, but physically unrealistic and heavily biased, case for assessing the effectiveness of equation (17); the crystal strains would be purely orientation-dependent and, for cubic symmetry, the dilatation would be homogeneous. Therefore, an elasto-viscoplastic FE-based modeling framework is used to generate a model LSDF (Marin & Dawson, 1998*a*).

In this framework, the aggregate is spatially discretized with FE, facilitating grain-to-grain interactions. Each discretized grain has three associated state variables: the slip system hardnesses, the elastic strain and the lattice orientation. Inelastic deformation is idealized as continuum slip: shearing takes place on the prescribed slip systems (determined by the crystal type) under the action of the resolved shear stresses. The elastic strain is related to the stress using anisotropic linear elasticity. The FE serve to partition the applied boundary conditions (velocities) over the aggregate and enforce compatibility on the deformation. Equilibrium is satisfied over the aggregate in a weak sense, using a Bubnov–Galerkin-type weighted residual of the field equations (Hughes, 2000). This differs from the elasto-viscoplastic extensions of Voight- or Reuss-type assumptions (*i.e.* one where all crystals experience either the applied deformation or the applied stress) where only compatibility or only equilibrium is satisfied. The net result of the intergranular interactions facilitated by the direct discretization of the aggregate is a more realistic description of the spatial variations in the strain/stress states among crystals having equivalent orientations. This modeling framework, as well as comparisons with others, has been described in detail (Marin & Dawson, 1998*a*,*b*; Han & Dawson, 2005).

A texture-free aggregate of 1000 Cu (face-centered cubic, f.c.c.) crystals was subjected to uniaxial tension to a macroscopic strain of ~2%. An LSDF was obtained directly from the individual crystal strains at the final load using a least-squares approach. A mesh containing 254 independent nodal points (399 total nodal points, 1512 elements) was used for representing the LSDF on the cubic $\Omega_{\rm fr}$. To keep the problem overdetermined, a DH expansion using the first 23 modes (corresponding to an order $L = 22$ for cubic symmetry) was employed for each component of ϵ. The SPF projection operators for the four lowest-order f.c.c. reflections were also calculated using a $10 \times 10^{\circ}$ grid (325 points) on the PF. As can be seen in comparing Figs. 1–5, the total range of variation in the dilatation field of the source LSDF is significantly smaller than the ranges of the tensor components, indicating a weak orientation dependence.

To assess the robustness of the proposed SPF inversion method, a set of simulated 'experimental' SPFs were obtained by perturbing the calculated SPFs with normally distributed noise. A standard deviation of 5×10^{-5} was chosen for the amplitude, in order to approximate the generally reported resolution limits for most experimental methods, which is $\sim 1 \times 10^{-4}$ (Withers *et al.*, 2001). Both sets of SPF data, the 'ideal' and 'noisy' variants, are shown in Fig. 6.

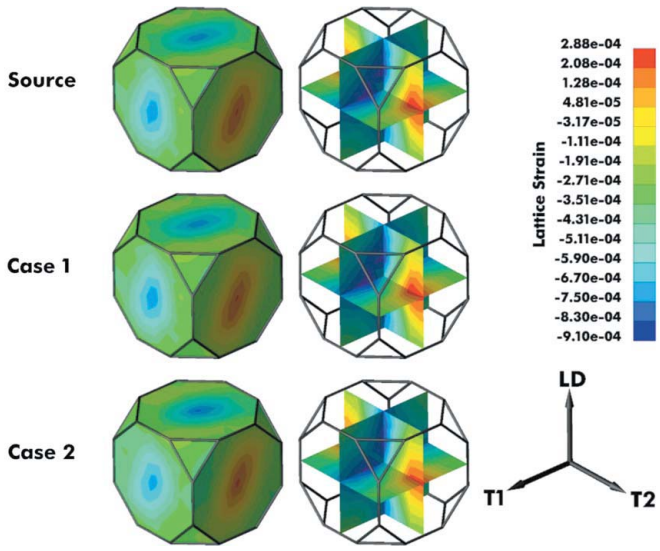

Figure 1
From top to bottom: ϵ_{22} from the source distribution, the optimal inversion of the ideal SPFs (Case 1) and the optimal inversion of the noisy variants (Case 2) plotted on the boundary and coordinate planes of the cubic $\Omega_{\rm fr}$. All components are shown in the sample-relative frame, where the loading direction is parallel to $\mathbf{x}_3$. The associated SPFs and component errors are shown in Fig. 6 and Table 2, respectively.

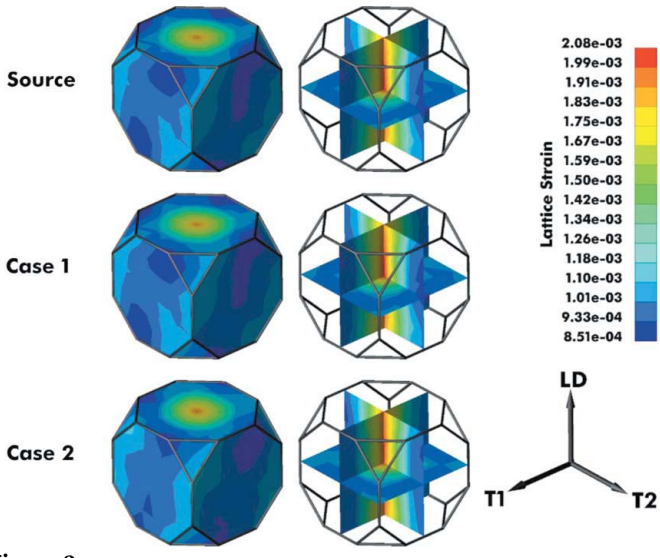

Figure 2
From top to bottom: ϵ_{33} from the source distribution, the optimal inversion of the ideal SPFs (Case 1) and the optimal inversion of the noisy variants (Case 2) plotted on the boundary and coordinate planes of the cubic $\Omega_{\rm fr}$. All components are shown in the sample-relative frame, where the loading direction is parallel to $\mathbf{x}_3$. The associated SPFs and component errors are shown in Fig. 6 and Table 2, respectively.

Both the ideal and the noisy SPF data are inverted for various $\alpha \in [0,\ 1]$, $\beta \in [0,\ 1000]$. For clarity, the inversion of the ideal SPFs will be referred to as 'Case 1' and the inversion of the noisy SPFs will be referred to as 'Case 2'. The parameter ranges were chosen to illustrate adequately the behavior of equation (17).

A discrete relative percent error measure (Matthies *et al.*, 1988),

$$\mathrm{RP}(I;\ x^{\mathrm{ref}},\ x^{\mathrm{cal}}) = 100 N_i^{-1} \sum_{i=1}^{N_i} \delta_i,$$
$$\text{where } \delta_i \equiv N_j^{-1} \sum_{\{j | x_i^{\mathrm{ref}}(j) > I\}} |x_i^{\mathrm{ref}}(j) - x_i^{\mathrm{cal}}(j)| / |x_i^{\mathrm{ref}}(j)|, \tag{22}$$

is employed to report errors between the source LSDF and the inversion results for each $(\alpha,\ \beta)$ pair for Case 1 and Case 2. For global errors, I in equation (22) is set to 0. Errors in the strain values above the noise amplitude, *i.e.* for $I = 5 \times 10^{-5}$, are also reported.

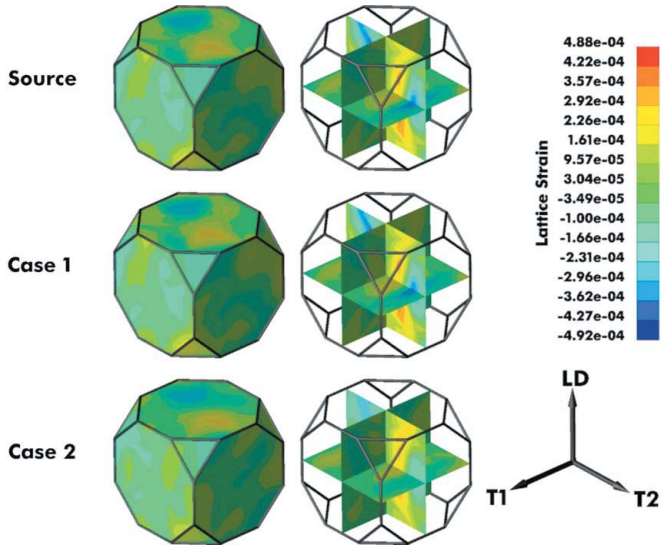

Figure 3
From top to bottom: ϵ_{13} from the source distribution, the optimal inversion of the ideal SPFs (Case 1) and the optimal inversion of the noisy variants (Case 2) plotted on the boundary and coordinate planes of the cubic Ω_{fr}. All components are shown in the sample-relative frame, where the loading direction is parallel to $\mathbf{x}_3$. The associated SPFs and component errors are shown in Fig. 6 and Table 2, respectively.

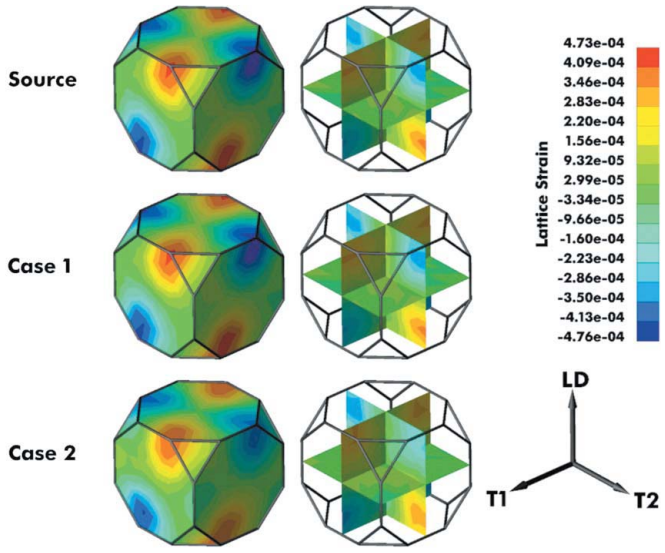

Figure 4
From top to bottom: ϵ_{12} from the source distribution, the optimal inversion of the ideal SPFs (Case 1) and the optimal inversion of the noisy variants (Case 2) plotted on the boundary and coordinate planes of the cubic Ω_{fr}. All components are shown in the sample-relative frame, where the loading direction is parallel to $\mathbf{x}_3$. The associated SPFs and component errors are shown in Fig. 6 and Table 2, respectively.

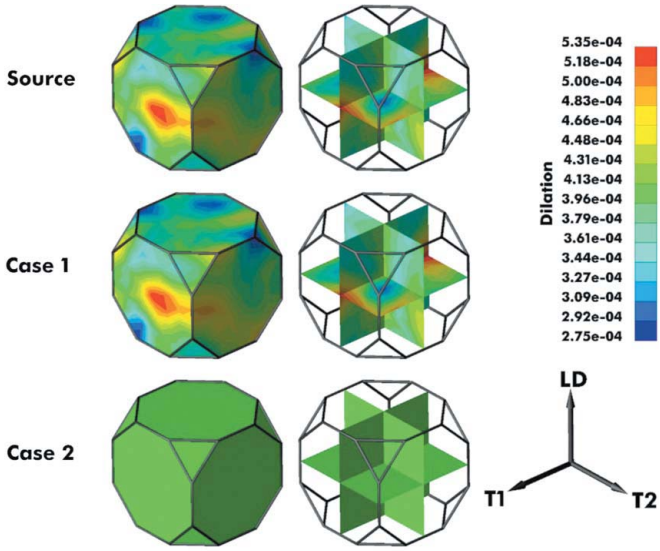

Figure 5
From top to bottom: $\mathrm{Tr}\,\boldsymbol{\epsilon}$ from the source distribution, the optimal inversion of the ideal SPFs (Case 1) and the optimal inversion of the noisy variants (Case 2). The total range of the dilatation from Case 2 is 1.28×10^{-6} despite the uniform appearance. The mean values of the distributions from top to bottom are 3.90×10^{-4}, 3.90×10^{-4} and 3.86×10^{-4}.

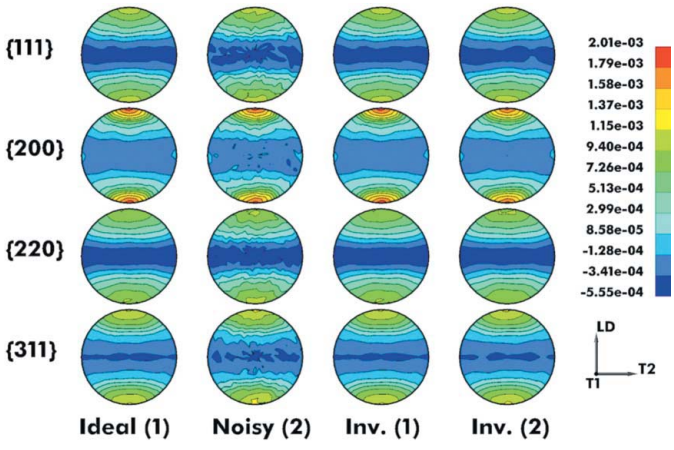

Figure 6
From left to right: equal-area projections of the synthetic SPFs from the source LSDF (1), the noisy variants (2), the reconstructed SPFs from the optimal inversion LSDFs using (1) and the reconstructed SPFs from the optimal inversion LSDFs using (2). Selected components of the associated LSDFs are shown in Figs. 1–4.

Table 1
Macroscopic stresses calculated from the simulation and LSDFs [see equation (6)].

Macrostress (MPa)	$\bar{\sigma}_{11}$	$\bar{\sigma}_{22}$	$\bar{\sigma}_{33}$	$\bar{\sigma}_{23}$	$\bar{\sigma}_{13}$	$\bar{\sigma}_{12}$
Simulation	−0.68	−0.07	160.97	0.82	0.58	0.10
Source LSDF	−0.68	−0.07	160.97	0.82	0.58	0.10
Case 1	−0.68	−0.07	160.97	0.82	0.58	0.10
Case 2	−0.65	−0.42	159.90	1.32	1.34	0.29

Table 2
Relative errors (RP_I) for the optimal LSDFs from Cases 1 and 2.

	ϵ_{11}	ϵ_{22}	ϵ_{33}	ϵ_{23}	ϵ_{13}	ϵ_{12}
$I = 0$						
Case 1 ($\times 10^{-9}$)	0.94	1.06	1.38	4.51	3.53	1.94
Case 2	10.26	12.33	4.72	37.48	43.83	23.00
$I = 5 \times 10^{-5}$						
Case 1 ($\times 10^{-9}$)	0.61	0.64	1.24	2.32	1.16	0.87
Case 2	6.30	6.00	4.12	13.57	30.83	10.50

Table 3
Relative errors (RP_I) for the principal strain magnitudes, $\epsilon_i^{\rm p}$, of the optimal LSDFs from Cases 1 and 2.

	$\epsilon 1^{\rm p}$	$\epsilon_2^{\rm p}$	$\epsilon_3^{\rm p}$
$I = 0$			
Case 1 ($\times 10^{-9}$)	0.77	1.94	1.34
Case 2	8.94	20.76	4.77
$I = 5 \times 10^{-5}$			
Case 1 ($\times 10^{-9}$)	0.52	0.77	1.21
Case 2	6.84	3.80	4.16

The optimal parameters, (α', β'), for Cases 1 and 2 were selected to minimize the global RP(0) errors for the LSDFs. The 22, 33, 13 and 12 components of the source LSDF, as well as those from the optimal Case 1 and Case 2 inversion LSDFs, are shown in Figs. 1–4, respectively. The reconstructed SPFs associated with the optimal Case 1 and Case 2 LSDFs are shown in Fig. 6. The macroscopic stresses calculated from the simulated data, the source LSDF and the optimal inversion LSDFs are listed in Table 1.

A comprehensive error analysis was performed on the results of the parameter study. Both the RP(0) and the RP(5×10^{-5}) errors for the LSDF components and principal strain values are listed in Tables 2 and 3, respectively. The errors for the corresponding SPFs are listed in Table 4. The complete set of RP(0) errors from the parameter study are also plotted as parametric surfaces in Figs. 7–10 to illustrate better the behavior of the SPF inversion method.

6. Results

6.1. Case 1: ideal SPFs

The inversion method captures the features of the source LSDF very well from the four ideal SPFs (Case 1), as evidenced by the component plots as well as the RP errors. The errors in the LSDF and reconstructed SPFs, listed,

Table 4
Relative errors (RP_I) for the reconstructed SPFs from Cases 1 and 2.

The SPF errors are calculated with respect to the corresponding input data, *i.e.* the ideal SPFs for Case 1 and the noisy variants for Case 2. The errors marked with an * are calculated with respect to the ideal SPFs.

	{111}	{200}	{220}	{311}
$I = 0$				
Case 1 ($\times 10^{-9}$)	1.20	1.30	1.26	0.96
Case 2	9.46	8.85	10.85	9.90
Case 2*	3.78	4.60	3.40	2.68
$I = 5 \times 10^{-5}$				
Case 1 ($\times 10^{-12}$)	8.06	7.32	9.79	7.03
Case 2	5.42	4.27	7.06	4.55
Case 2*	2.02	3.24	1.89	1.61

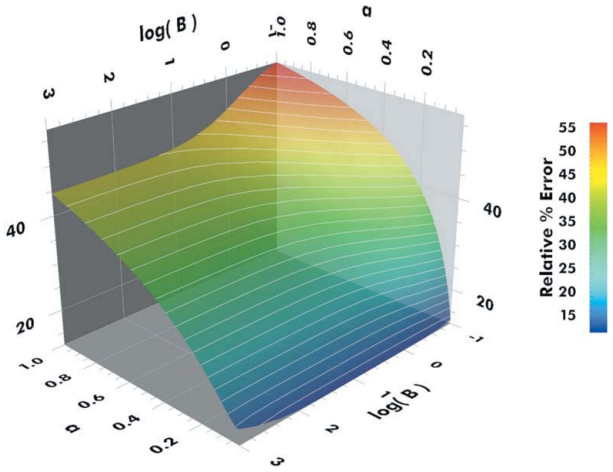

Figure 7
Parametric surface showing the relative percent errors between the source LSDF and the inversion LSDFs from the ideal SPFs (Case 1) for $\alpha \in (0, 1]$ and $\beta \in (0, 1000]$. The optimal parameter values for this case are $(\alpha', \beta') = (0.0, 0.0)$. The associated SPFs and LSDF components are shown in Fig. 6 and Figs. 1–4, respectively.

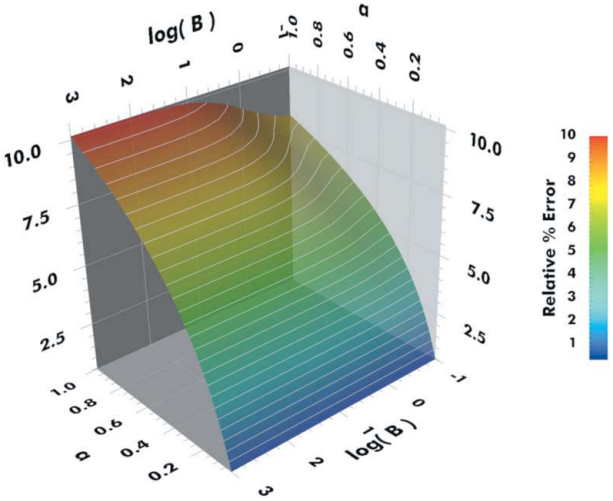

Figure 8
Parametric surface showing the relative percent errors between the input and reconstructed SPFs from Case 1, for $\alpha \in (0, 1]$ and $\beta \in (0, 1000]$. The associated SPFs and LSDF components are shown in Fig. 6 and Figs. 1–4, respectively.

respectively, in Tables 2 and 4, are unilaterally near machine precision. Plots of the ϵ_{11} and ϵ_{23} components have been omitted for brevity since they are closely related to the ϵ_{22} and ϵ_{13} components in terms of ranges, errors and general topographies. The macroscopic stresses obtained from the inversion LSDF are also in excellent agreement with the simulation results, as shown in Table 1. Such small discrepancies are not surprising, considering that the numerical system is overdetermined by a factor of about four.

The behavior of the solution to equation (17) with increasing α and β is illustrated by Figs. 7 and 8. One salient feature in Fig. 7 is the relative insensitivity of the mean global errors to changes in the dilatation parameter β for values greater than $\sim$10; these errors are a much stronger function of the stability parameter, α. A similar trend is apparent in Fig. 8. As the strengths of the coupling parameters are increased, the relative priority of the SPF residual in equation (17) is lowered, which in turn leads to solutions with increasingly large SPF errors. The optimal parameter values, (α', β'), are (0, 0) for Case 1, that is, the solution having the smallest SPF residual errors also has the smallest LSDF component errors. This result is attributable to two features: the overdetermined nature of the problem, and the fact that the indeterminacy of equation (12) is not represented in the FE/Rodgriues discretization of equation (17). The SPF inversion becomes a fairly well conditioned least-squares problem in this case without the need for conditional control of the solution *via* the stability and dilatation smoothing terms.

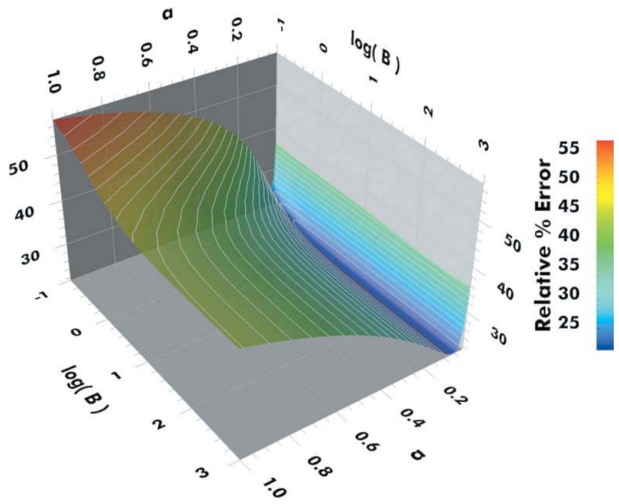

Figure 9
Parametric surface showing the relative percent errors between the source LSDF and the inversion LSDFs from the noisy SPFs (Case 2) for $\alpha \in (0, 1]$ and $\beta \in (0, 1000]$. The optimal parameter values for this case are $(\alpha', \beta') = (0.06, 100)$. The associated SPFs and LSDF components are shown in Fig. 6 and Figs. 1–4, respectively.

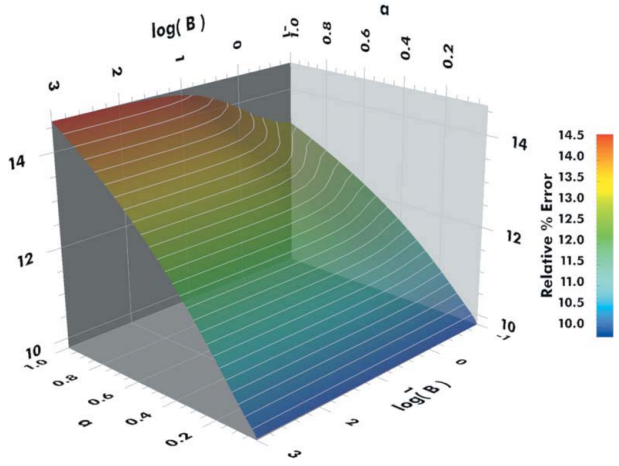

Figure 10
Parametric surface showing the relative percent errors between the input and reconstructed SPFs from Case 2, for $\alpha \in (0, 1]$ and $\beta \in (0, 1000]$. The associated SPFs and LSDF components are shown in Fig. 6 and Figs. 1–4, respectively. The percent increase in the mean error for the SPFS at the optimal (α, β) is 9.91%.

6.2. Case 2: noisy SPFs

The results for Case 2 show some significant differences from the previous case. Case 2 represents the more interesting case for the purpose of processing experimentally measured SPFs. The importance of the conditional α and β terms for handling noisy SPF data is apparent in Fig. 11, which shows the ϵ_{22}, ϵ_{33} and ϵ_{23} components obtained from the noisy SPFs using α, $\beta = 0$. The selected components bear little or no resemblance to the corresponding components of the source LSDF, despite the fact that this LSDF provides the smallest SPF residual errors for Case 2. Similarly to the Case 1 results, the RP(0) errors on the LSDF for Case 2 (see Fig. 9) are a more sensitive function of α than of β. The error magnitude does not, however, monotonically increase with α and β for Case 2. Each $\beta =$ constant section through the error surface has a single critical value of α. Furthermore, these critical values change very little as a function of β, leading to the 'trough' in Fig. 9. The optimal coupling parameter values for

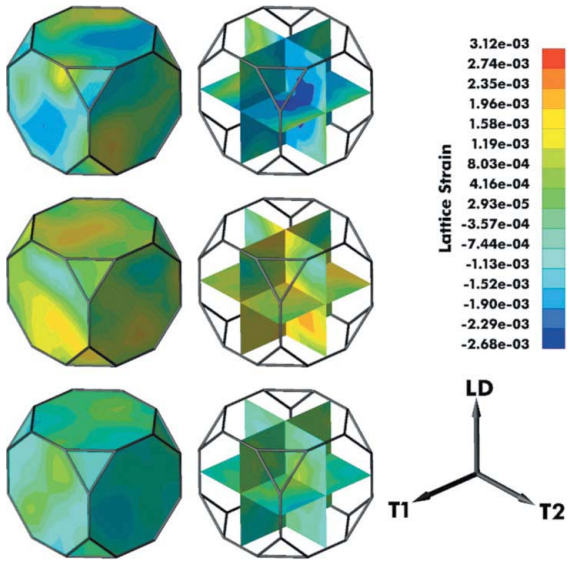

Figure 11
From top to bottom: ϵ_{22}, ϵ_{33} and ϵ_{13} from inversion of the noisy variants (Case 2) using $(\alpha, \beta) = (0, 0)$. A comparison to the corresponding Case 2 components in Figs. 1–3 reveals the importance of the conditional control of the solution when dealing with noisy SPF data.

Case 2 are (0.06, 100.0); however, there is little change in the quality of the solutions for $\beta > 10$.

The LSDF components having the largest magnitudes, *i.e.* the diagonal components, are captured with the smallest errors, as shown in Table 2. This trend is clearer when examining the principal strains at each orientation. The errors between the principal strain magnitudes for each case and the source LSDF, shown in Table 3, closely resemble the errors from the diagonal components. The errors for both the normal and the principal components are significantly smaller than those in the shears, despite the fact that the overall topographies of the recovered shears are in good agreement with those from the source distribution (see Figs. 3 and 4). The overall range of the shears for the Case 2 LSDF are slightly smaller than the source distribution. This behavior is in part due to the stability term in equation (17). For fixed $\beta > 0$, the effect of increasing α is a general smoothing of the components, particularly in the vicinity of extrema and in regions where the absolute magnitudes are less than the SPF noise amplitude. The latter effect is clear in Table 4.

Another salient source of discrepancy can be traced to the volumetric component of the inversion LSDF. Fig. 5 shows the dilatation of the source and optimal inversion LSDFs. For the noisy SPF data (Case 2), the optimal solution has a nearly uniform dilatation centered on the corresponding mean value of the source LSDF. This discrepancy is apparent in the global RP(0) errors of the principal values. However, the largest errors occur in strains smaller than the 'resolution limit' imposed by the noise on the data, as evidenced by the significant drop in magnitudes between the RP(0) and RP(5×10^{-5}) errors.

The SPF errors for Case 2 (Fig. 11) follow a similar trend to those from Case 1, although with larger magnitudes owing to the incompatibilities in the input SPFs. In contrast to Case 1, the solution that minimizes the LSDF errors does not simultaneously minimize the SPF residual. For the optimal solution, the mean SPF errors [RP(0)] are 9.91% larger than the (0, 0) solution. This behavior, in conjunction with the relative insensitivity of solution accuracy to increasing β, supports the use of a selection criteria in which β is set to be large relative to α, while α is optimized such that the relative increase in the mean SPF error remains below 10%. For reference, the SPF errors are calculated with respect to the input (noisy) SPFs as well as the ideal SPFs from Case 1. The latter errors, marked with an * in Table 4, are smaller than those calculated with respect to the input SPF data. Further analysis has shown that the optimal LSDF solution for the noisy input data does produce the minimum SPF errors, as calculated with respect to the underlying ideal SPFs from Case 1 rather than the input data.

7. Discussion

The complete results for Case 2 suggest that the fidelity of quantitative strain analysis is highly sensitive to the quality of the experimental data. To compound the problem, only sparse SPF coverage is available to most experimental techniques. In these cases, assumptions regarding the statistical symmetries of the sample, reinforced by simulated data, may be exploited to reduce the indeterminacy of the SPF inversion problem. The SPFs are roughly axisymmetric in the provided example, following from the symmetry of the applied macroscopic deformation. The FE/Rodrigues implementation facilitates an elegant geometric representation of the symmetries *via* nodal point equivalences. The presented SPF inversion method is also versatile in that it may handle arbitrary SPF coverage without modification or the need for data manipulation *a priori*.

The empirical results using the model LSDF suggest that the optimal solution, in the presence of experimental errors, is qualitatively the smoothest LSDF that best captures the noise-free SPFs and mean dilatation. A qualitative explanation for the gradual increase in the LSDF errors with increasing α and β is related to a topological smoothing of the trial solutions. While the overall ranges of the components become compressed, the relative positions of the extrema remain unaffected.

The α term is clearly critical in terms of filtering experimental noise. The effect of the β term on the LSDF errors is much more subtle for the case presented. This fact is most likely attributable to the relatively homogeneous dilatation in the simulated LSDF. However, as discussed in §4.1, this behavior is generally expected in the materials for which this analysis is most relevant, such as structural alloys.

The presented method for LSDF analysis provides a distribution of mean orientation-dependent crystal strains. It is acknowledged that in a deformed polycrystal the strain/stress in crystals having equivalent orientations will in general differ as a result of intergranular interactions. Therefore it may be desirable in future work to include information regarding the orientation-dependent variance of the crystal strains in the definition of the LSDF. This information is theoretically available *via* analysis of the diffraction peak profiles (Young, 1995; Cullity, 1978). The combination of the two fields, mean and variance, could provide a more complete, stochastic description of the micromechanical state of a sample. This method could also be implemented within a Rietveld refinement package, such as *MAUD* (Lutterotti, 2000; Chateigner, 2006), in a manner analogous to that of direct PDF inversion methods (Wenk *et al.*, 2003; Ischia *et al.*, 2005).

8. Conclusions

A versatile and robust direct method is presented for obtaining the orientation-dependent distribution of intergranular elastic strains in polycrystalline samples from diffraction strain pole figures. Heuristics for selecting the optimal coupling parameters in the auxiliary problem are also presented, based on the results of a parameter study using simulated SPF data. The parameter study using the provided model LSDF suggests that the optimal solution to the SPF inversion problem

(i) is smooth,

(ii) matches the input data well, and

(iii) captures the average dilatation over the polycrystal.

In addition, the FE/Rodrigues framework employed for the representation of the LSDF has several distinct benefits, including

(i) versatility,

(ii) the straightforward application of symmetries, and

(iii) the ability to handle arbitrary SPF coverage.

The software used for this analysis will be made available upon request in the form of a Matlab function library.

This work was sponsored (in part) by the Air Force Office of Scientific Research, USAF, under grant/contract number F49620-02-1-0047. The authors thank Tong-Seok Han for providing the FE simulation data and Donald Boyce, Paul Dawson, Hadas Ritz, Jae-Hyung Cho, Jon Almer and Ulrich Lienert for many valuable discussions regarding this work.

References

Barton, N. R., Boyce, D. E. & Dawson, P. R. (2002). *Textures Microstruct.* **35**, 113–144.

Behnken, H. (2000). *Phys. Status Solidi. A*, **177**, 401–418.

Bernier, J. V., Boyce, D. E. & Miller, M. P. (2006). *J. Appl. Cryst.* Submitted.

Bunge, H. J. (1982). *Texture Analysis in Materials Science*. London: Butterworth.

Caleyo, F., Baudin, T., Mathon, M. H. & Penelle, R. (2001). *Eur. Phys. J. AP*, **15**, 85–96.

Carter, D. H. & Bourke, M. A. M. (2000). *Acta Mater.* **31**(A), 1543–1555.

Chateigner, D. (2006). *Combined Analysis: Structure–Texture–Microstructure–Phase–Stresses–Reflectivity Determination by X-rays and Neutron Scattering*. Available online at http://www.ecole.ensicaen.fr/∼chateign/texture/combined.pdf.

Cullity, B. D. (1978). *Elements of X-ray Diffraction*, 2nd ed. Reading, MA: Addison-Wesley.

Dawson, P. R., Boyce, D. E., MacEwen, S. & Rogge, R. (2001). *Mater. Sci. Eng. A*, **313**, 123–144.

Dawson, P. R., Miller, M. P., Han, T. S. & Bernier, J. V. (2005). *Met. Trans. A*, **36**, 1627–1641.

Frank, F. C. (1988). *Met. Trans. A*, **19**, 403–408.

Han, T. S. & Dawson, P. R. (2005). *Mater. Sci. Eng. A*, **13**, 203–223.

Hauk, V. (1997). *Structural and Residual Stress Measurement by Nondestructive Methods*. Amsterdam: Elsevier.

Heinz, A. & Neumann, P. (1991). *Acta Cryst.* A**47**, 780–789.

Hughes, T. J. R. (2000). *The Finite Element Method: Linear Static and Dynamic Finite Element Analysis*, ch. 3. New York: Dover.

Ischia, G., Wenk, H. R., Lutterotti, L. & Berberich, F. (2005). *J. Appl. Cryst.* **38**, 377–380.

Johnson, C. (1992). *Numerical Solution of Partial Differential Equations by the Finite Element Method*. Cambridge University Press.

Kallend, J. S. (2000). *Texture and Anisotropy: Preferred Orientations in Polycrystals and their Effect on Materials Properties*, edited by U. F. Kocks, C. N. Tomé & H. R. Wenk, ch. 3, pp. 102–125. Cambridge University Press.

Kumar, A. & Dawson, P. (1998). *Comput. Methods Appl. Mech. Eng.* **153**, 259–302.

Lu, J. (1996). Editor. *Handbook of Measurements of Residual Stresses*. Bethel, CT: Society of Experimental Mechanics.

Lutterotti, L. (2000). *Acta Cryst.* A**56** (Suppl.), s54.

Margulies, L., Lorentzen, T., Poulsen, H. F. & Leffers, T. (2002). *Acta Mater.* **50**, 1771–1779.

Marin, E. B. & Dawson, P. R. (1998*a*). *Comput. Methods Appl. Mech. Eng.* **165**, 1–21.

Marin, E. B. & Dawson, P. R. (1998*b*). *Comput. Methods Appl. Mech. Eng.* **165**, 23–41.

Matthies, S. & Vinel, G. (1982). *Phys. Status Solidi B*, **112**, K111–K120.

Matthies, S., Wenk, H.-R. & Vinel, G. W. (1988). *J. Appl. Cryst.* **21**, 285–304.

Miller, M. P., Bernier, J. V., Park, J. S. & Kazimirov, A. Y. (2005). *Rev. Sci. Instrum.* **76**, 1–11.

Morawiec, A. & Field, D. P. (1996). *Philos. Mag. A*, **73**, 1113–1130.

Popa, N. C. & Balzar, D. (2001). *J. Appl. Cryst.* **34**, 187–195.

Poulsen, H. F., Nielsen, S. F., Lauridsen, E. M., Schmidt, S., Suter, R. M., Lienert, U., Margulies, L., Lorentzen, T. & Jensen, D. J. (2001). *J. Appl. Cryst.* **34**, 751–756.

Schaeben, H. (1991). *J. Appl. Phys.* **69**, 1320–1329.

Van Houtte, P. (1984). *Textures Microstruct.* **6**, 137–162.

Wang, Y. D. (2000). *ECRS 5: Proceedings of the Fifth European Conference on Residual Stresses*, edited by A. J. Bèottger, R. Delhez & E. J. Mittemeijer, Vol. 347, pp. 66–71. Delft: Noordwijkerhout.

Wang, Y. D., Lin Peng, R. & McGreevy, R. L. (2001). *Philos. Mag. Lett.* **81**, 153–163.

Wang, Y. D., Lin Peng, R., Wang, X.-L. & McGreevy, R. L. (2002). *Acta Mater.* **50**, 1717–1734.

Wang, Y. D., Wang, X.-L., Stoica, A. D., Richardson, J. W. & Lin Peng, R. (2003). *J. Appl. Cryst.* **36**, 14–22.

Wanner, A. & Dunand, D. (2000). *Metall. Mater. Trans. A*, **31**, 2949–2962.

Wenk, H.-R., Lutterotti, L. & Vogel, S. (2003). *Nuclear Instrum. Methods Phys. Res. Sect. A*, **515**, 575–588.

Withers, P. J., Daymond, M. R. & Johnson, M. W. (2001). *J. Appl. Cryst.* **34**, 737–743.

Young, R. A. (1995). Editor. *The Rietveld Method*. IUCr/Oxford University Press.